

PolSAM: Polarimetric Scattering Mechanism Informed Segment Anything Model

Yuqing Wang^{a,b}, Zhongling Huang^{a,b,*}, Shuxin Yang^a, Hao Tang^c, Xiaolan Qiu^{d,e}, Junwei Han^a and Dingwen Zhang^{a,b,*}

^athe BRain and Artificial INtelligence Lab (BRAIN LAB), School of Automation, Northwestern Polytechnical University, Xi'an, 710072, China

^bthe Shenzhen Research Institute of Northwestern Polytechnical University, Shenzhen, 518057, China

^cthe National Key Laboratory for Multimedia Information Processing, School of Computer Science, Peking University, Beijing, 100871, China

^dthe National Key Laboratory of Microwave Imaging Technology, Chinese Academy of Sciences, Beijing, 100090, China

^ethe Aerospace Information Research Institute, Chinese Academy of Sciences, Beijing, 100094, China

ARTICLE INFO

Keywords:

PolSAR terrain segmentation, prompt-based fusion learning, segment anything model, physical scattering characteristic.

ABSTRACT

PolSAR data presents unique challenges due to its rich and complex characteristics. Existing data representations, such as complex-valued data, polarimetric features, and amplitude images, are widely used. However, these formats often face issues related to usability, interpretability, and data integrity. While most feature extraction networks for PolSAR attempt to address these issues, they are typically small in size, which limits their ability to effectively extract features. To overcome these limitations, we introduce the large, powerful Segment Anything Model (SAM), which excels in feature extraction and prompt-based segmentation. However, SAM's application to PolSAR is hindered by modality differences and limited integration of domain-specific knowledge. To address these challenges, we propose the Polarimetric Scattering Mechanism-Informed SAM (PolSAM), which incorporates physical scattering characteristics and a novel prompt generation strategy to enhance segmentation performance with high data efficiency. Our approach includes a new data processing pipeline that utilizes polarimetric decomposition and semantic correlations to generate Microwave Vision Data (MVD) products, which are lightweight, physically interpretable, and information-dense. We extend the basic SAM architecture with two key contributions: The Feature-Level Fusion Prompt (FFP) module merges visual tokens from the pseudo-colored SAR image and its associated MVD, enriching them with supplementary information. When combined with a dedicated adapter, it addresses modality incompatibility in the frozen SAM encoder. Additionally, we propose the Semantic-Level Fusion Prompt (SFP) module, a progressive mechanism that leverages semantic information within MVD to generate sparse and dense prompt embeddings, refining segmentation details. Experimental evaluation on the newly constructed PhySAR-Seg datasets shows that PolSAM outperforms existing SAM-based models (without MVD) and other multimodal fusion methods (with MVD). The proposed MVD enhances segmentation results by reducing data storage and inference time, outperforming other polarimetric feature representations. The source code and data will be publicly available at <https://github.com/XAI4SAR/PolSAM>.

1. Introduction

Polarimetric Synthetic Aperture Radar (PolSAR) provides rich polarization features that enable detailed representation of terrain and ground targets, offering enhanced accuracy and feature discrimination for applications such as land-cover segmentation [Tirandaz et al. \(2020\)](#); [Bi et al. \(2020\)](#); [Wang et al. \(2022\)](#). Recently, deep learning-based methods for PolSAR image segmentation have gained significant attention. These approaches typically reformat PolSAR data into specific input representations and design specialized neural networks to extract both spatial and polarimetric features [Liu et al. \(2018\)](#); [Zhang et al. \(2020b\)](#); [Qin et al. \(2020\)](#); [Ghanbari et al. \(2023\)](#). Common input representations include complex-valued data [Li et al. \(2020\)](#), model-based polarimetric features [Antropov et al. \(2013\)](#); [Shen et al. \(2020\)](#); [Ghanbari et al. \(2023\)](#), and amplitude images [Pu et al. \(2024\)](#). These are processed using various

architectures, including complex-valued neural networks (CVNNs) [Yu et al. \(2022\)](#); [Kuang et al. \(2024\)](#), convolutional neural networks (CNNs) [Liu et al. \(2018\)](#); [Ghanbari et al. \(2023\)](#); [Zhang et al. \(2020b\)](#), Transformers [Hua et al. \(2024\)](#), and graph neural networks (GNNs) [Dong et al. \(2021\)](#); [Jamali et al. \(2023\)](#). However, these input formats present challenges in terms of usability, interpretability, and data integrity. Moreover, the existing models are typically of limited scale, which constrains their representational capacity.

As illustrated in Fig. 1(a), complex-valued inputs preserve the complete information of PolSAR data but require substantially high storage capacity. Furthermore, their processing necessitates the use of specialized CVNNs, which introduces additional computational complexity and reduces interpretability. This constraint also limits the applicability of existing large-scale vision models, as they are primarily designed to handle real-valued data, making the integration of complex-valued inputs challenging. Model-based polarimetric features enhance the interpretability of complex-valued PolSAR data, enabling effective integration with popular deep learning architectures such as CNNs,

*Corresponding author

✉ huangzhongling@nwpu.edu.cn (Z. Huang);
zhangdingwen2006yyy@gmail.com (D. Zhang)

ORCID(s):

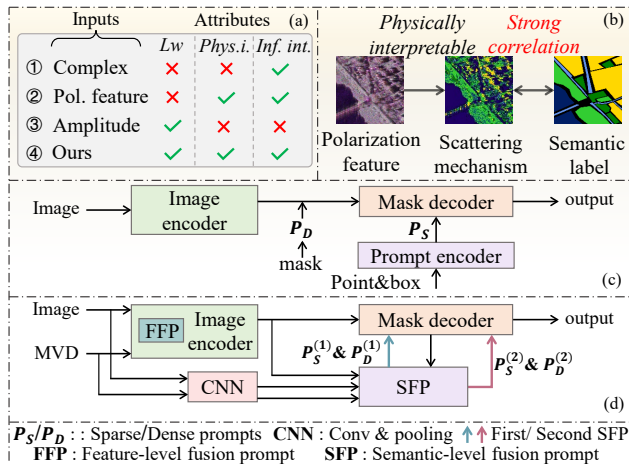


Figure 1: (a) Different input representations of PolSAR data and their corresponding attributes, including lightweight (Lw), physical interpretability (Phys. i.), and information integrity (Inf. int.), are explored. (b) Scattering mechanisms depict polarization characteristics with physical interpretability and exhibit a strong correlation with semantic information. (c) Original SAM architecture; (d) Our PolSAM model.

Transformers, and GNNs; however, these features are also high-dimensional. The most widely used format is the 8-bit quantized amplitude PolSAR image, which aligns with photographic conventions for compatibility with existing deep learning models Zhang et al. (2020a); Liu et al. (2022); Zhang et al. (2023b). Nevertheless, this approach sacrifices rich polarimetric features, resulting in significant information loss. Investigating a user-friendly input format for PolSAR data that retains comprehensive polarimetric information is essential for deep learning applications.

In PolSAR image segmentation, these challenges become more severe due to limited data availability. This constraint particularly affects networks with fewer parameters, which often fail to extract sufficient information from input data. Knowledge transfer from pre-trained models offers a common solution Wu et al. (2019), yet the high dimensionality of polarimetric features frequently renders them incompatible with standard image representations Huang et al. (2018). Although CVNNs possess twice the parameters of traditional real-valued networks, the absence of effective pre-trained models constrains their utility. In data-scarce scenarios, CVNNs frequently encounter convergence difficulties, further limiting their practical applicability Zeng et al. (2022, 2023). Despite various advanced architectures proposed to address these challenges, the inherent constraints of small network architectures impede effective feature extraction. Moreover, the diversity of PolSAR datasets, variations in scattering mechanisms, and differences in imaging conditions complicate the development of models capable of robust performance across diverse scenarios Ghanbari et al. (2023).

To address these challenges, this work designs an efficient input format for PolSAR data that integrates Pauli pseudo-colored images with inherent scattering properties,

preserving essential polarimetric features for analysis. Previous studies Hua et al. (2024); Huang et al. (2022) have established the critical importance of scattering mechanisms in PolSAR analysis. As illustrated in Fig. 1(b), we optimize scattering properties into a compact image format that reduces storage requirements while maintaining intuitive physical interpretability. Notably, specific scattering patterns correspond directly to particular land cover categories, revealing strong correlations with semantic label information. Building on this foundation, we develop a generalized segmentation framework for PolSAR images that harnesses the robust capabilities of existing large vision models. This approach bridges the gap between PolSAR data's unique characteristics and the superior generalization ability of advanced large vision models, enabling broader applications and enhanced usability for non-expert users.

Building on these insights, we introduce the Segment Anything Model (SAM) Kirillov et al. (2023), as shown in Fig. 1(c). First, SAM leverages its large-scale architecture and robust data processing capabilities to achieve efficient and precise segmentation across diverse image content, making it a promising pre-trained foundation model for PolSAR applications. Second, SAM's prompt-based segmentation mechanism effectively incorporates high-level external prompts, guiding the model to focus on relevant features. This capability is particularly well-suited for compact, high-level scattering mechanism data, providing semantic guidance to enhance segmentation accuracy.

Overall, we propose the Polarimetric Scattering Mechanism-Informed SAM (PolSAM). We first introduce a novel data product, Microwave Vision Data (MVD), which represents compact scattering mechanism classifications. Based on the above description, MVD is lightweight, physically interpretable, and information-dense. Then, to integrate physical scattering properties into SAM, we use two key modules, as shown in Fig. 1(d). The Feature-Level Fusion Prompt (FFP) module first merges patch embeddings from the Pauli decomposition-based pseudo-colored image and MVD, enhancing their interaction before feeding into the SAM encoder. Dedicated adapters in each encoder layer address modality incompatibility in the frozen SAM encoder, fostering feature complementarity. The Semantic-Level Fusion Prompt (SFP) module, second, refines semantic guidance for segmentation through a two-stage process. First, it integrates input features with encoder outputs; then, it aligns the fused representations with high-level semantic prompts, boosting segmentation performance.

Our contributions are as follows:

1. We propose a novel pipeline for PolSAR data that generates user-friendly, physically interpretable, and information-dense MVD products. These lightweight products leverage the strong correlation between scattering mechanisms and semantics to aid in terrain segmentation.
2. We propose PolSAM, a SAM-based PolSAR segmentation method that combines PolSAR domain-specific knowledge with SAM's strengths to improve efficiency

and accuracy. PolSAM includes FFP, which fuses Pauli pseudo-colored images and MVD embeddings for better feature complementarity, and SFP, which uses a two-level design to refine semantic prompts through enhanced input and high-level semantic feature interaction.

- Experiments on the PhySAR-Seg datasets show that PolSAM outperforms SAM-based and multimodal fusion models. The sparse and dense prompts effectively capture semantic relevance, guiding segmentation tasks. Additionally, MVD integration reduces storage requirements, offering a more efficient alternative to traditional polarimetric representations.

2. Related Works

2.1. Deep learning based PolSAR image analysis

Deep learning techniques have become essential in PolSAR image analysis, leveraging their advanced information processing capabilities to improve segmentation performance [Liu et al. \(2018\)](#); [Zhang et al. \(2020b\)](#); [Qin et al. \(2020\)](#); [Ghanbari et al. \(2023\)](#). Currently, widely used methods include CNNs or Transformer-based architectures, GNNs, and CVNNs. The inputs processed by these methods can be broadly classified into three categories: complex-valued data, model-based polarimetric features, and simple amplitude data.

As shown in Fig. 1(a), "✓" denotes an affirmative indicator, "✗" denotes a negative indicator. Complex-valued data is mainly processed using CVNNs [Li et al. \(2020\)](#); [Yu et al. \(2022\)](#); [Kuang et al. \(2024\)](#). Clearly, this approach satisfies information integrity (Inf. int.), but it requires high storage and computational resources, making it not lightweight (Lw), while also lacking physical interpretability (Phys. i.). Polarimetric features (Pol. feature), which mainly include Pauli decomposition-based features [Antropov et al. \(2013\)](#), polarization coherence matrix T [Shen et al. \(2020\)](#); [Gao et al. \(2023\)](#); [Zhang et al. \(2023d\)](#), polarization covariance matrix C [Ghanbari et al. \(2023\)](#); [Xiang et al. \(2024\)](#), and scattering features extracted from traditional polarization decomposition methods such as Cloude-Pottier, H/A/Alpha decomposition, Freeman-Durden three-component decomposition, and Yamaguchi four-component decomposition, provide physically interpretable and relatively rich information. These features enhance the ability of deep learning models to interpret PolSAR data [Xiao et al. \(2020\)](#); [Shi et al. \(2023\)](#). However, they are remain high-dimensional, resulting in high storage and computational costs, making them not lightweight. In comparison, amplitude data, typically represented as 8-bit quantized grayscale images or pseudo-colored images visualized using different polarization modes (HH, HV, VH), is lightweight but suffers from significant information loss and lacks physical interpretability [Pu et al. \(2024\)](#). In summary, these methods face challenges in simultaneously achieving lightweight representation, physical interpretability, and information richness.

Polarimetric features and amplitude data formats can both be processed using networks such as CNNs, Transformers, and GNNs. CNNs and Transformers aim to capture fundamental structural and texture details by enhancing polarization feature representation through advanced techniques [Liu et al. \(2018\)](#); [Ghanbari et al. \(2023\)](#); [Zhang et al. \(2020b\)](#); [Hua et al. \(2024\)](#); [Zhang et al. \(2023d\)](#). GNNs optimize spatial relationships in PolSAR images by modeling complex spatial dependencies and integrating multi-scale information [Geng et al. \(2022\)](#); [Shi et al. \(2023\)](#); [Wang et al. \(2024\)](#). Despite the aforementioned advancements, these networks often require task-specific designs and their limited scale restricts scalability and computational efficiency.

It is worth noting that existing deep learning models do not directly process the classification results of scattering mechanisms but instead focus on scattering features extracted by traditional decomposition methods. The MVD product we propose represents the classification results of scattering mechanisms, providing higher-level physical information that not only offers better physical interpretability but also has a strong correlation with semantic information. As shown in Fig. 1(a), ours, which combines MVD with Pauli pseudo-colored images, achieves a lightweight, user-friendly representation while preserving physical interpretability and information integrity.

2.2. SAM Implementation in Segmentation

The SAM model has demonstrated considerable success in segmentation tasks, primarily due to its large model size, which enables powerful feature extraction and broad applicability. Additionally, its flexible prompt-based segmentation mechanism allows it to effectively handle external high-level prompt information [Zhang et al. \(2023e,a\)](#); [Wu et al. \(2023\)](#); [Chai et al. \(2023\)](#). This versatility has driven adoption across diverse domains, including natural images [Zhang et al. \(2023a,e\)](#); [Ke et al. \(2024\)](#), medical imaging [Wu et al. \(2023\)](#); [Chai et al. \(2023\)](#); [Yue et al. \(2023, 2024\)](#); [Xu et al. \(2024b,a\)](#), and remote sensing [Chen et al. \(2024\)](#); [Zhang et al. \(2024a\)](#); [Yan et al. \(2023\)](#); [Zheng et al. \(2024\)](#); [Ma et al. \(2024\)](#); [Zhou et al. \(2024\)](#). In medical imaging and remote sensing, where modality differences necessitate tailored approaches, researchers have adapted SAM with specialized adapter techniques [Wu et al. \(2023\)](#); [Zhang et al. \(2024a\)](#); [Pu et al. \(2024\)](#). Further refinements, such as integrating text prompts within segmentation modules, have also enhanced its performance [Yue et al. \(2023\)](#). For natural images, innovations explore the use of a multi-modal encoder that combines visual and linguistic information to generate prompt embeddings [Zhang et al. \(2024b\)](#), while PAM-SAM [Xie et al. \(2024\)](#) introduces a prompt-driven adapter to enhance SAM's mask quality by refining sparse and dense prompt features. Altogether, these adaptations highlight SAM's capacity for domain-specific adjustments, extending its applications across diverse image types.

PolSAR data's scattering mechanism classification results are high-level compared to polarimetric and scattering features, and SAM's strengths are well-suited to address the

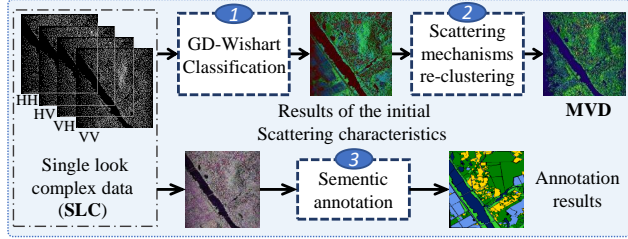


Figure 2: Data processing pipeline: unsupervised GD-Wishart classification, MVD generation through re-clustering of scattering mechanisms, and semantic annotation, illustrated with the PhySAR-Seg-1 dataset.

challenges we previously outlined. However, despite many of the above methods effectively adjusting SAM, it still faces challenges when applied to PolSAR images, mainly due to modality differences and the inability to integrate domain-specific knowledge. For this, our model introduces two specialized prompt learning modules: one enhances feature complementarity through early-stage fusion of SAR and MVD embeddings, while the other generates precise sparse and dense prompts through a two-level fusion of features and semantic context, effectively guiding the decoder in the segmentation process.

3. PhySAR-Seg Dataset

To tackle the data challenges mentioned above, we propose a novel pipeline for constructing the PhySAR-Seg dataset. The key innovation is Microwave Vision Data (MVD), a lightweight and user-friendly representation that ensures high storage efficiency and provides intuitive, physically interpretable visualizations of scattering mechanisms. By integrating MVD with Pauli pseudo-colored images, we also ensure information integrity. Details of the pipeline and dataset are provided below.

3.1. PhySAR-Seg Dataset Processing Pipeline

The dataset processing pipeline involves three key steps: (1) Polarimetric decomposition and unsupervised GD-Wishart classification of PolSAR images; (2) MVD generation by re-clustering the physical scattering mechanisms based on semantic correlations; and (3) Manual annotation. Fig. 2 illustrates the entire process, using the PhySAR-Seg-1 dataset as an example.

In the first step, we generate pseudo-colored images from original single look complex (SLC) data using the Pauli decomposition algorithm, which extracts three components and assigns them to RGB channels respectively [Huang et al. \(2021\)](#). Subsequently, the SLC data undergoes processing with the GD-Wishart classification algorithm [Ratha et al. \(2017\)](#) to produce initial clustering results. Targets are categorized into three primary classes: odd-bounce, double-bounce, and volume scattering. In practical experiments, double-bounce scattering occurs infrequently and is represented by a single class, while odd-bounce and volume categories are each subdivided into five sub-classes.



Figure 3: Semantic label clustering of data PhySAR-Seg-1.

To better align MVD with semantic information, we re-cluster scattering classes by grouping sub-classes within each primary category based on semantic correlations. Beyond the three primary scattering types, the dataset incorporates mixed and 'other' classes, with the latter typically containing boundary pixels of undefined scattering characteristics. Through color-coding and cluster visualization, we generate MVD as a compact and informative representation of scattering mechanisms. This representation enables efficient large-scale processing, provides intuitive electromagnetic property visualization, and preserves physical meaning while optimizing storage requirements and enhancing interpretability for subsequent analysis.

3.2. Datasets Description

Based on this processing pipeline, we construct two lightweight, physically interpretable, and information-integrated PhySAR-Seg datasets, each comprising paired pseudo-colored and MVD images. Their comprehensive representation capabilities provide a solid foundation for evaluating our proposed method.

The PhySAR-Seg-1 dataset derives from [Yan et al. \(2024\)](#) and includes L, S, C, and X bands covering the same geographic region. The L, S, and C bands achieve 0.5 m resolution, while the X band provides 1.0 m resolution. Fig. 4 presents a dataset overview, displaying pseudo-colored images, MVD, and label maps alongside both MVD and semantic legends. In the MVD legend, colors within identical hues represent consistent scattering types, with lighter shades indicating higher SPAN values. The semantic legend shows proportions of five final terrain classes, clearly illustrating their distribution. Initially containing 14 land cover types, we merge these into five categories: urban surfaces, water, buildings, barren land, and vegetation, as shown in Fig. 3. We calculate MVD for each band, with comparative analysis revealing optimal X-band performance. Since all bands cover identical regions and capture similar scattering mechanisms, we register X-band MVD to the remaining three bands for final result generation. The segmented dataset contains 2,866 pseudo-colored MVD image pairs, each measuring 512 × 512 pixels. We partition data from each band into training, validation, and test sets using a 6:2:2 ratio, following the dashed lines in Fig. 4. This strategy ensures that data from

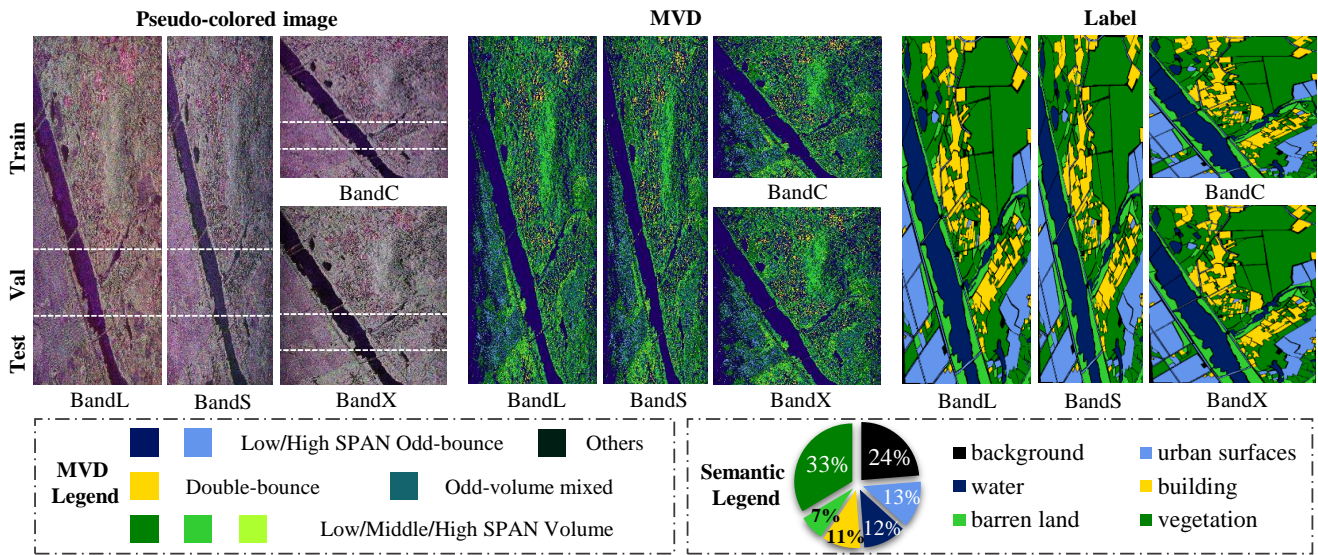


Figure 4: Visualization of the PhySAR-Seg-1 dataset, including the pseudo-colored image, MVD, semantic label, MVD legend, and semantic legend. The white dashed lines on the pseudo-colored image divide the dataset into train, val, and test sets.

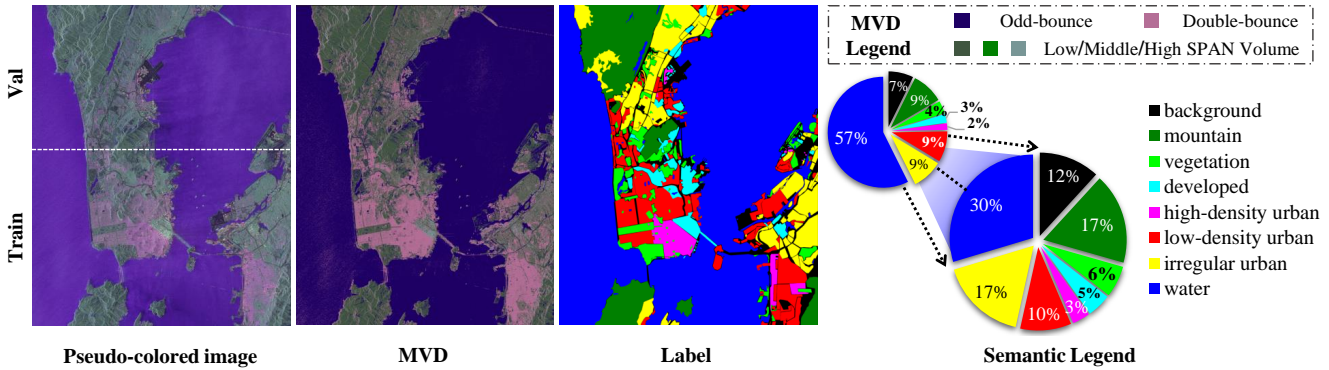


Figure 5: Visualization of the PhySAR-Seg-2 dataset, including the pseudo-colored image, MVD, semantic label, MVD legend, and semantic legend. The white dashed line on the pseudo-colored image divide the dataset into train and val sets.

identical geographic regions across different bands remains within the same set, preventing overlap between training, validation, and test partitions.

The PhySAR-Seg-2 dataset derives from [Gaofen-3 \(2019\)](#) and utilizes spaceborne C-band data. We obtain MVD following the methodology in Fig. 2, while labels are acquired through manual annotation, yielding seven categories excluding background. Fig. 5 presents the dataset overview, displaying pseudo-colored images, MVD, and corresponding semantic labels. Due to limited sample availability, we partition the data into training and validation sets using a 6:4 ratio, as indicated by the dashed line in the figure. Given the substantial water presence in the dataset, we strategically remove pure water samples from the segmented 512×512 images to maintain categorical balance. Following this adjustment, 1,110 images remain, with 668 assigned to training and 442 to validation. The semantic legend clearly illustrates category distribution before and after processing.

4. The Proposed Method

4.1. Revisiting SAM

SAM introduces an innovative prompt-based architecture for diverse segmentation tasks, comprising three main components: the image encoder (f_{Enc}), prompt encoder (f_{PE}), and mask decoder (f_{Dec}). The image encoder extracts high-dimensional feature maps from input images, establishing the foundation for SAM's segmentation capabilities. The prompt encoder serves a pivotal role by processing flexible inputs including sparse prompts (I_{sparse} , such as points or bounding boxes), dense prompts (I_{dense} , such as masks), and text. These prompts direct the model toward specific regions of interest and are transformed into embeddings that integrate with image features. The mask decoder subsequently fuses both sparse and dense embeddings with image features to generate final segmentation masks. This architecture enables SAM to address diverse segmentation challenges effectively without requiring task-specific fine-tuning, providing a versatile and robust solution across various scenarios. The

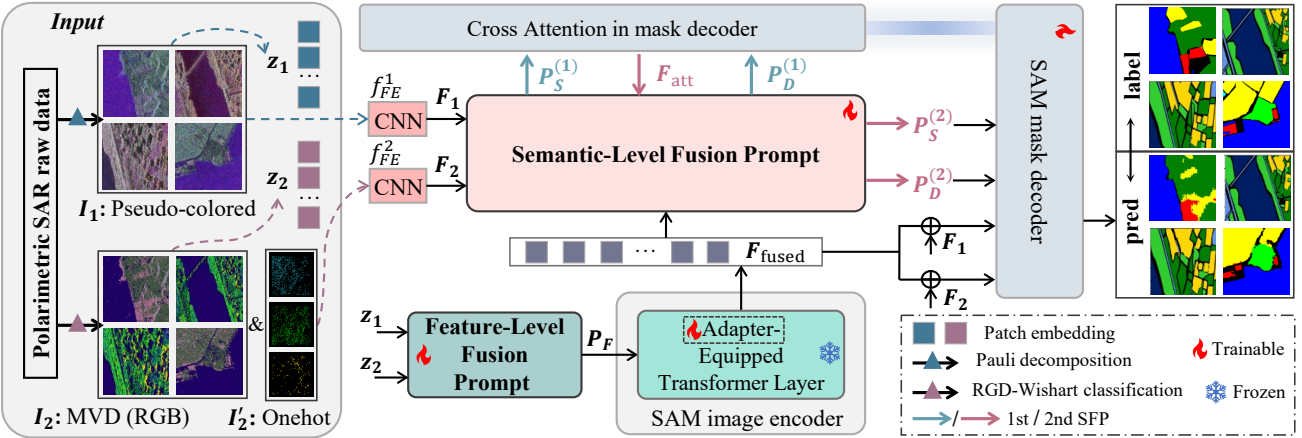


Figure 6: Overview of the proposed PolSAM. It consists of a novel data product, MVD, a Feature-Level Fusion Prompt (FFP) module and a progressive Semantic-Level Fusion Prompt (SFP) module. MVD is lightweight, encapsulates physical information, and correlates with semantic information. The FFP module combines data in a trainable manner for initial integration, while the SFP module generates sparse and dense prompts through a progressive two-level information interaction, guiding the segmentation task. By leveraging domain-specific knowledge of PolSAR data, PolSAM achieves enhanced segmentation performance with high data efficiency.

process can be mathematically represented as follows:

$$\begin{aligned} \mathbf{F}_{\text{img}} &= f_{\text{Enc}}(\mathbf{I}), \\ \mathbf{P}_s, \mathbf{P}_d &= f_{\text{PE}}(\mathbf{I}_{\text{sparse}}, \mathbf{I}_{\text{dense}}), \\ \mathbf{M} &= f_{\text{Dec}}(\mathbf{F}_{\text{img}}, \mathbf{P}_s, \mathbf{P}_d), \end{aligned} \quad (1)$$

where \mathbf{I} represents the input image, \mathbf{F}_{img} is the image feature map extracted by the image encoder. $\mathbf{P}_s, \mathbf{P}_d$ represent the sparse prompt embeddings and dense prompt embeddings. \mathbf{M} is the final segmentation mask produced by the mask decoder.

Building on SAM’s success in segmentation, we adopt its image encoder and mask decoder as our network backbone while keeping the encoder frozen. Inspired by SAM’s prompt-based mechanism that utilizes geometric prompts such as points, boxes, or masks, we propose a novel approach for autonomous semantic prompt generation. By incorporating domain-specific cues, our method produces both sparse and dense semantic prompts, enabling effective leverage of task-specific and data-specific information for enhanced segmentation performance. The detailed architecture is described below.

4.2. PolSAM Overview

Fig. 6 illustrates the overview of our proposed PolSAM. We adopt SAM’s image encoder (f_{Enc}) and mask decoder (f_{Dec}) while preserving their original structures. Pseudo-colored images provide rich texture details and strong visual representation, whereas MVD captures scattering mechanisms and conveys semantic information. To effectively exploit and integrate these data-specific features, we propose the Feature-Level Fusion Prompt (FFP) module, positioned before the image encoder to fuse features from both inputs for comprehensive representation. Additionally, to address data modality incompatibility and enhance encoder adaptation to

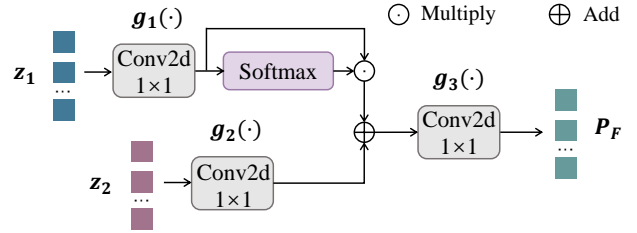


Figure 7: Detailed design of module FFP.

PolSAR data, we introduce trainable adapter modules into each layer of the frozen image encoder, improving feature representation and segmentation performance.

To provide effective semantic prompts to the decoder, we design a progressive Semantic-Level Fusion Prompt (SFP) module. Each level targets distinct aspects of key information, enabling nuanced semantic integration. The process is described by the following equations:

$$\begin{aligned} \mathbf{F}_{\text{fused}} &= f_{\text{FFP}}(\mathbf{f}_{\text{FFP}}(\mathbf{I}_1, \mathbf{I}_2)), \\ \mathbf{P}_s, \mathbf{P}_d &= f_{\text{SFP}}(\mathbf{I}_1, \mathbf{I}'_2), \\ \mathbf{M} &= f_{\text{Dec}}(\mathbf{F}_{\text{fused}}, \mathbf{P}_s, \mathbf{P}_d), \end{aligned} \quad (2)$$

where, f_{FFP} and f_{SFP} represent the FFP and SFP modules, respectively. \mathbf{I}_1 denote the pseudo-colored image, \mathbf{I}_2 and \mathbf{I}'_2 represent MVD in RGB and one-hot form respectively. In the following sections, we will analyze each module in details.

4.3. Feature-Level Fusion Prompt

The FFP design follows the concept proposed in Jia et al. (2022), where a lightweight convolutional module is inserted at the image encoder’s beginning. Here, the pseudo-colored image and MVD image are denoted as \mathbf{I}_1 and \mathbf{I}_2 respectively, with corresponding patch embeddings

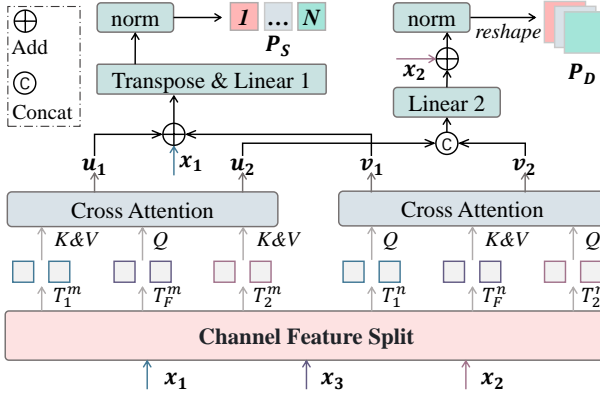


Figure 8: Detailed design of the proposed SFP: $\mathbf{P}_S \in \mathbb{R}^{N \times C}$ and $\mathbf{P}_D \in \mathbb{R}^{H \times W \times C}$ represent sparse prompts and dense prompts, respectively.

\mathbf{z}_1 and \mathbf{z}_2 . Given these inputs' distinct characteristics, \mathbf{z}_1 relates closely to local details and image texture, while \mathbf{z}_2 reflects scattering mechanisms more associated with semantic information. Therefore, enhancing \mathbf{z}_1 's spatial resolution is essential for emphasizing local details, whereas \mathbf{z}_2 undergoes direct dimensionality reduction to preserve global semantic features.

As illustrated in Fig. 7, FFP takes \mathbf{z}_1 and \mathbf{z}_2 as input and performs dimension reduction using 1×1 convolutions to obtain latent features for each input. The latent features of \mathbf{z}_1 are then processed with Softmax activation across spatial dimensions to emphasize important regions, followed by multiplication to enhance these areas. Subsequently, the fused features are projected back to their original dimension using 1×1 convolutions, yielding the initial fusion prompt at the feature level. Here, $g_1(\cdot)$, $g_2(\cdot)$, and $g_3(\cdot)$ represent the three convolution layers. The fusion prompt can thus be derived as:

$$\begin{aligned} \mathbf{P}_F &= f_{\text{FFP}}(\mathbf{z}_1, \mathbf{z}_2) \\ &= g_3(g_1(\mathbf{z}_1) \odot \text{Softmax}(g_1(\mathbf{z}_1)) + g_2(\mathbf{z}_2)). \end{aligned} \quad (3)$$

4.4. Adapter-Equipped Image Encoder

The resulting \mathbf{P}_F is then combined with \mathbf{z}_1 and \mathbf{z}_2 to form the input for the pre-trained image encoder. The encoder backbone remains frozen during training, while we apply the adapter technology proposed in Wu et al. (2023) within each encoder layer to adapt feature extraction. This approach enables the fusion prompt and adapters to learn complementarity between different inputs through fine-tuning of only a few parameters. The acquisition of $\mathbf{F}_{\text{fused}}$ can thus be detailed as presented in Equation (2):

$$\mathbf{F}_{\text{fused}} = f_{\text{Enc}}(\mathbf{P}_F, \mathbf{z}_1, \mathbf{z}_2). \quad (4)$$

4.5. Semantic-Level Fusion Prompt

Inspired by SAM's promptable mechanism, we propose the SFP module that generates sparse and dense prompt

embeddings to guide segmentation. Featuring a two-level progressive structure, SFP optimizes feature integration and enhances semantic representation. This design balances extraction of unique and complementary information from different inputs, enriching the segmentation process. Through progressive feature interaction refinement, the SFP module significantly improves segmentation accuracy and contextual awareness.

First, pseudo-colored images I_1 are processed using a basic convolutional block and two pooling layers to obtain feature embedding \mathbf{F}_1 , denoted as $f_{\text{FE}}^1(\cdot)$, as shown in Fig. 6. Given the strong correlation between MVD and semantic labels, we directly adopt the CNN network from SAM's prompt encoder for processing mask prompts. This network sequentially downsamples input through three convolution layers with intermediate normalization and activation functions, reducing input channels and mapping final output to the target embedding dimension. To ensure semantic prompts remain unaffected by color encoding, we directly use the one-hot form of MVD, denoted as I'_2 , to obtain feature embedding \mathbf{F}_2 , represented by $f_{\text{FE}}^2(\cdot)$. Features \mathbf{F}_1 and \mathbf{F}_2 share the same dimension as $\mathbf{F}_{\text{fused}}$. This process can be denoted as:

$$\mathbf{F}_1 = f_{\text{FE}}^1(I_1), \quad \mathbf{F}_2 = f_{\text{FE}}^2(I'_2). \quad (5)$$

The proposed SFP follows a progressive process with two levels implemented using a shared module. For clarity, we denote them as SFP-1 and SFP-2. As shown in Fig. 6, each SFP level receives three inputs, denoted as $f_{\text{SFP}}(\mathbf{x}_1, \mathbf{x}_2, \mathbf{x}_3)$. SFP-1 takes individual input embeddings \mathbf{F}_1 and \mathbf{F}_2 , along with the fused encoder feature $\mathbf{F}_{\text{fused}}$, to output initial sparse and dense prompts $\mathbf{P}_{S,D}^{(1)}$. To generate more specific semantic prompts, SFP-2 additively combines single-input features with fusion features and interacts with semantic features \mathbf{F}_{att} from the mask decoder attention layer to produce final sparse and dense prompts $\mathbf{P}_{S,D}^{(2)}$, where $\mathbf{P}_S \in \mathbb{R}^{N \times C}$ and $\mathbf{P}_D \in \mathbb{R}^{H \times W \times C}$. This process can be denoted as:

$$\begin{aligned} \mathbf{P}_{S,D}^{(1)} &= f_{\text{SFP}}(\mathbf{F}_1, \mathbf{F}_2, \mathbf{F}_{\text{fused}}), \\ \mathbf{P}_{S,D}^{(2)} &= f_{\text{SFP}}(\mathbf{F}_{\text{fused}} + \mathbf{F}_1, \mathbf{F}_{\text{fused}} + \mathbf{F}_2, \mathbf{F}_{\text{att}}), \end{aligned} \quad (6)$$

Fig. 8 shows the SFP details. Given three arbitrary inputs $\mathbf{x}_1, \mathbf{x}_2, \mathbf{x}_3 \in \mathbb{R}^{C \times H \times W}$, channel feature split is applied to obtain two feature groups with identical dimensions $\mathbb{R}^{C \times H \times W}$, denoted as $[T_1^m, T_2^m, T_3^m]$ and $[T_1^n, T_2^n, T_3^n]$ respectively. This is realized through a linear layer that increases dimension from C to $2C$. By exchanging query and value, two groups of enhanced features are obtained using cross-attention modules, denoted as $[v_1, v_2]$ and $[u_1, u_2]$, with dimension $H \times W \times C$. The sparse and dense prompts are then generated separately through the following operations:

$$\begin{aligned} \mathbf{P}_S &= \text{Norm}(\text{Linear}_1(0.5(v_1 + u_1) + \text{DimTrans}(x_1))) \\ \mathbf{P}_D &= \text{Norm}(\text{Linear}_2(\text{Concat}(v_2, u_2)) + \text{DimTrans}(x_2)), \end{aligned} \quad (7)$$

where $\text{Norm}(\cdot)$, $\text{Concat}(\cdot)$, and $\text{DimTrans}(\cdot)$ denote the normalization, concatenation, and dimension transformation, respectively. The linear mappings $\text{Linear}_1(\cdot)$ and $\text{Linear}_2(\cdot)$ aim to map the dimension from HW to N , from $2C$ to C , respectively.

From the above descriptions, the SFP module aims to fuse different inputs interactively, enriching information to a considerable extent. The two cross-attention modules treat different inputs as queries to obtain attention weights for feature enhancement. In SFP-1, \mathbf{F}_1 , \mathbf{F}_2 , and $\mathbf{F}_{\text{fused}}$ correspond to x_1 , x_2 , and x_3 respectively. Consequently, u_1 and u_2 demonstrate that fusion features for segmentation ($\mathbf{F}_{\text{fused}}$) are enhanced by single-input features, while v_1 and v_2 indicate remarkable single-input features attended by fusion information. The initial sparse and dense semantic prompts pass through the cross-attention module in the mask decoder to output \mathbf{F}_{att} , representing high-level semantic features. In SFP-2, u_1 , u_2 and v_1 , v_2 indicate results of mutual enhancement between fusion information and high-level semantic features.

The SFP module enhances feature representation through interactive input fusion and progressive semantic prompt refinement. This approach preserves critical details while enriching the feature space. Furthermore, mutual enhancement between fused information and high-level semantic features improves model understanding, leading to superior segmentation results.

4.6. Loss Function

The feature embedding of single and fused inputs are then added together as the input of mask decoder, as well as the sparse and dense semantic prompt. Finally, the segmentation result y can be obtained as:

$$y = f_{\text{Dec}}(\mathbf{F}_1, \mathbf{F}_2, \mathbf{F}_{\text{fused}}, \mathbf{P}_{\text{S/D}}). \quad (8)$$

Based on extensive experimental comparisons, we use the cross-entropy loss function for the PhySAR-Seg-1 dataset, which is defined as:

$$\mathcal{L}_{\text{CE}} = - \sum_{i=1}^N y_i \log(\hat{y}_i), \quad (9)$$

where y_i , \hat{y}_i are the true label and predicted probability for class i , and N is the number of samples.

For the PhySAR-Seg-2 dataset, where class distribution is more imbalanced, we adopt focal loss to calculate the loss function. The weight for each category is the inverse of its dataset proportion, enhancing the model's focus on harder-to-classify, less frequent categories. The focal loss is given by:

$$\mathcal{L}_{\text{FL}} = - \sum_{i=1}^N w_i (1 - \hat{y}_i)^\gamma y_i \log(\hat{y}_i), \quad (10)$$

where $w_i = \frac{1}{p_i}$ is the weight for class i (with p_i being the proportion of class i), γ is the focusing parameter to down-weight easy examples, y_i is the true label, and \hat{y}_i is the predicted probability for class i .

5. Experiments and Discussions

This section presents experimental configuration, results analysis, and discussions, including metric comparisons and visualization interpretations. It encompasses ablation studies on module design, evaluation of semantic prompt effectiveness, hyperparameter analysis of sparse prompts, and discussion on MVD effectiveness.

5.1. Experimental Settings

Implementation Details. The pre-trained ViT-B model in SAM serves as our encoder backbone. The framework is trained using the AdamW optimizer with $\beta_1 = 0.9$ and $\beta_2 = 0.999$. We set the batch size to 12, epochs to 350, and the initial learning rate to 0.001. A 4% training warm-up is applied, followed by exponential decay of the learning rate with a factor of 0.9. Experiments are conducted on a single NVIDIA 4090Ti GPU.

Evaluation Metrics. Following existing methods, we apply three common overall metrics to evaluate the results of the semantic segmentation, including mean pixel accuracy (mAcc), mean F1 score (mF1 score), and mean intersection over union (mIoU). Additionally, for each class, we use the IoU as the evaluation metric.

5.2. Comparison With State-of-the-art Methods

We compare PolSAM with ten state-of-the-art (SOTA) image segmentation methods across both datasets. First, we evaluate PolSAM using only pseudo-colored images (denoted as PolSAM w/o MVD) and compare it with five SAM-based methods, including those using optical [Ke et al. \(2024\)](#); [Chai et al. \(2023\)](#); [Zhang et al. \(2023a,e\)](#) and remote sensing images [Zhang et al. \(2024a\)](#), since the original SAM accepts only single inputs. Additionally, we compare PolSAM with five multimodal fusion algorithms [Reza et al. \(2024\)](#); [He et al. \(2023\)](#); [Zhou et al. \(2021\)](#); [Zhang et al. \(2023c\)](#); [Zhou et al. \(2023\)](#), as our method uses two inputs. The results are presented in Tables 1 and 2. The following is a detailed description of the results of the experiment.

Evaluation Metrics. For the PhySAR-Seg-1 dataset (Table 1), PolSAM outperforms other advanced SAM-based methods for both natural and remote sensing images. Specifically, PolSAM (w/o MVD) surpasses the top-performing method, RSAM-Seg [Zhang et al. \(2024a\)](#), with improvements of 1.44% in mAcc, 1.7% in mF1 score, and 2.09% in mIoU. Additionally, PolSAM shows significant superiority over other multimodal fusion methods, achieving SOTA performance.

For the PhySAR-Seg-2 dataset (Table 2), the SAM-LST method [Chai et al. \(2023\)](#) achieves the best performance among SAM-based approaches, with an mIoU of 42.82%. In comparison, PolSAM (w/o MVD) achieves 45.30%, improving by 2.48%. Due to the distinct nature of SAR data, existing SAM-based models struggle with optimal performance. PolSAM also outperforms multimodal fusion methods, achieving 0.48% higher mF1 and 2.38% better mIoU than GMNet [Zhou et al. \(2021\)](#), showcasing its effectiveness with diverse data inputs.

Table 1

Comparison of PolSAM performance on the PhySAR-Seg-1 dataset: methods above the dashed line are SAM-based, while those below are multimodal. Metrics include per-category IoU and overall performance. Best results are highlighted in bold, second-best are underlined, and complete PolSAM is marked in red.

Models	IoU Per Category (%)						Overall Metrics (%)		
	BK	Urban surfaces	Water	Building	Barren land	Vegetation	mAcc	mF1 score	mIoU
Personalize-SAM	HQ-SAM Ke et al. (2024)	22.05	4.92	10.76	1.05	1.01	27.34	31.49	25.70
	SAM-LST Chai et al. (2023)	32.26	60.20	79.60	57.80	54.73	66.14	72.72	72.70
	Mobile-SAM Zhang et al. (2023e)	44.65	65.12	83.99	60.93	73.29	69.8	78.26	79.39
	RSAM-Seg Zhang et al. (2024a)	22.91	52.09	77.28	42.85	44.24	55.62	64.18	64.84
	PolSAM(w/o MVD)	51.22	69.64	86.45	68.98	78.52	76.21	82.62	83.37
	MMSFormer Reza et al. (2024)	46.19	68.79	85.14	63.35	67.57	72.64	79.52	80.03
GMNet	SFAF-MA He et al. (2023)	54.29	73.03	87.56	69.41	77.07	76.99	83.67	84.33
	CMX Zhang et al. (2023c)	45.41	65.11	50.03	53.05	65.16	70.74	75.96	75.62
	LSNet Zhou et al. (2023)	36.52	65.07	46.87	63.58	64.5	60.18	69.15	73.24
	PolSAM(w/ MVD)	55.44	73.97	87.97	69.62	78.66	75.65	83.70	84.71
	PolSAM(w/o MVD)	51.22	69.64	86.45	68.98	78.52	76.21	82.62	83.37
	PolSAM(w/ MVD)	55.44	73.97	87.97	69.62	78.66	75.65	83.70	84.71

Table 2

Comparison of PolSAM performance on the PhySAR-Seg-2 dataset.

Models	IoU Per Category (%)								Overall Metrics (%)		
	BK	Montain	Vegetation	Developed	I-urban	H-urban	L-urban	Water	mAcc	mF1 score	mIoU
Personalize-SAM	HQ-SAM Ke et al. (2024)	7.91	15.89	0.77	0.11	0.00	6.88	7.98	44.71	29.69	21.88
	SAM-LST Chai et al. (2023)	29.22	78.26	18.27	15.55	27.44	32.67	47.75	93.38	74.19	58.29
	Mobile-SAM Zhang et al. (2023e)	28.61	65.63	14.68	5.74	1.74	32.06	47.06	94.62	70.24	50.39
	RSAM-Seg Zhang et al. (2024a)	28.86	68.54	13.18	5.91	1.98	33.98	50.74	93.87	70.76	49.07
	PolSAM(w/o MVD)	35.00	77.15	21.07	16.27	34.16	35.08	50.91	92.76	74.31	59.03
	MMSFormer Reza et al. (2024)	30.84	72.00	14.28	8.60	0.00	37.93	44.60	93.80	72.24	51.51
GMNet	SFAF-MA He et al. (2023)	32.78	81.39	17.74	12.39	5.82	33.28	52.62	94.54	74.49	52.69
	CMX Zhang et al. (2023c)	31.75	82.73	24.75	16.17	11.08	36.39	55.23	95.22	77.31	60.92
	LSNet Zhou et al. (2023)	29.21	73.12	14.20	22.02	2.14	36.93	41.32	94.90	69.75	53.84
	PolSAM(w/ MVD)	34.83	75.88	22.63	18.13	30.76	42.43	54.57	93.31	76.47	61.40
	PolSAM(w/o MVD)	35.00	77.15	21.07	16.27	34.16	35.08	50.91	92.76	74.31	59.03
	PolSAM(w/ MVD)	34.83	75.88	22.63	18.13	30.76	42.43	54.57	93.31	76.47	61.40

Additionally, the metrics for each category of the two datasets are visualized in Fig. 9, providing a clear comparison of the results. The blue bars represent our PolSAM(w/o MVD) method, corresponding to the blue-themed SAM-based approaches, while the red bars indicate our PolSAM(w/

MVD) method, aligned with the red-themed multimodal methods. Our method demonstrates three key strengths. First, both PolSAM (w/ MVD) and PolSAM (w/o MVD) outperform other methods across most categories. Second, PolSAM (w/ MVD) consistently surpasses PolSAM (w/o

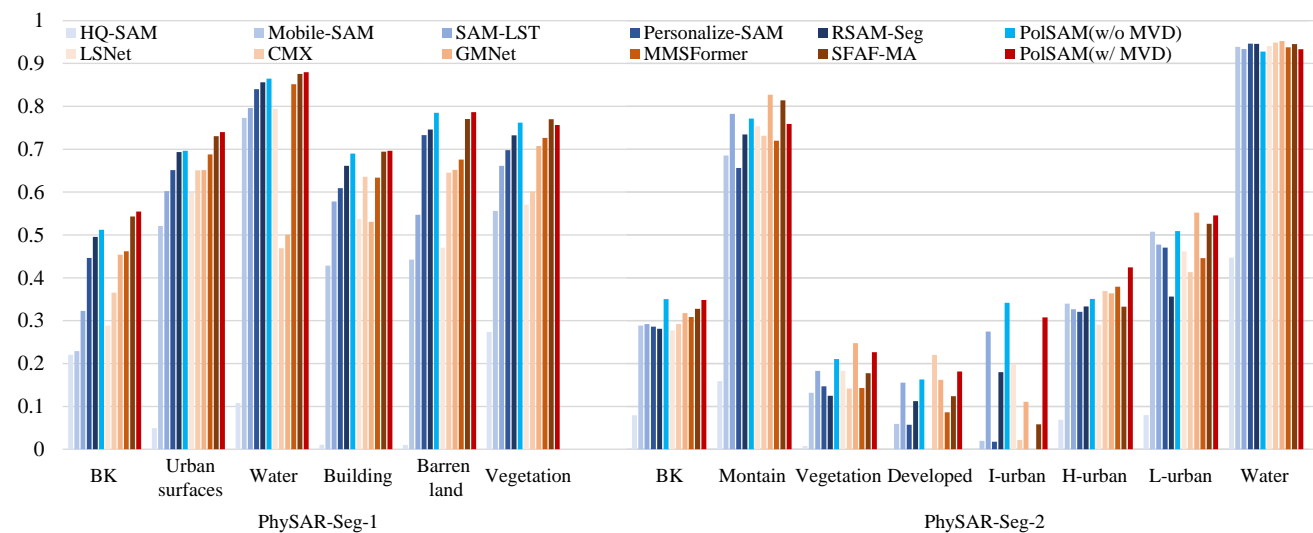


Figure 9: Comparison of IoU metrics for each category across different models on two datasets. The left side corresponds to the PhySAR-Seg-1 dataset, and the right side corresponds to the PhySAR-Seg-2 dataset.

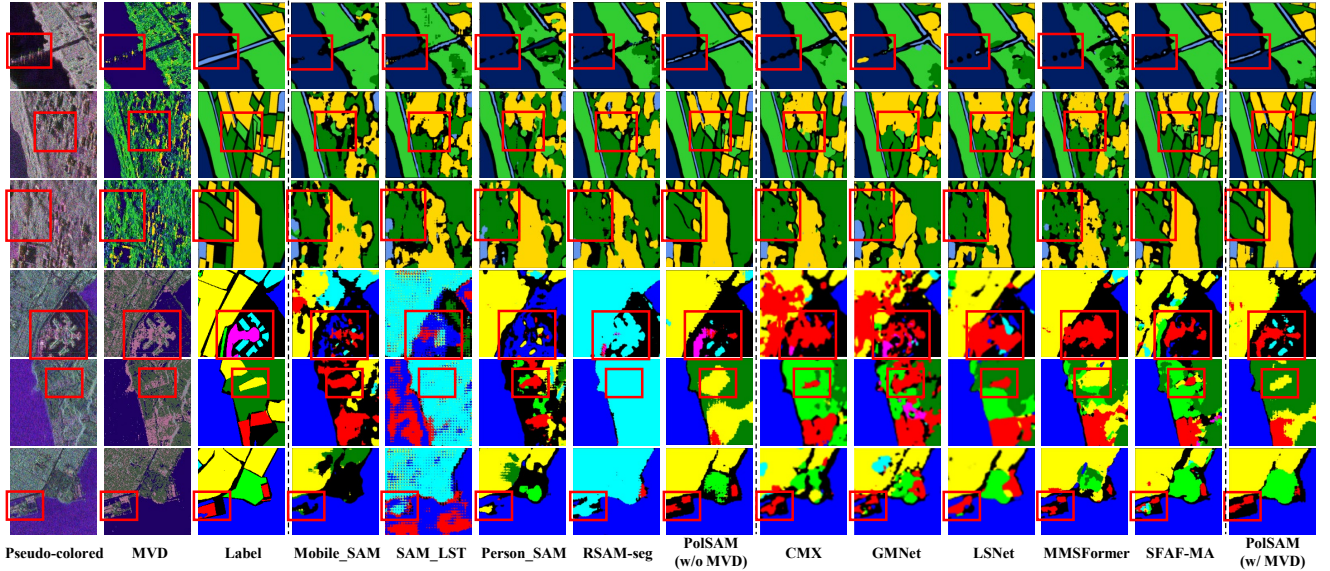


Figure 10: Visualization of segmentation results on the PhySAR-Seg-1 (rows 1-3) and PhySAR-Seg-2 (rows 4-6) datasets: each row displays a randomly selected image from the test set, while each column shows results from different models.

MVD), demonstrating the benefits of incorporating MVD. Third, PolSAM achieves optimal results across nearly all categories for the PhySAR-Seg-1 dataset. For the PhySAR-Seg-2 dataset, it shows significant improvement, particularly in the urban class where double-bounce scattering dominates despite small class proportion. This demonstrates that leveraging MVD in challenging scenarios substantially enhances segmentation accuracy.

Visualization. Fig. 10 presents segmentation results for the PhySAR-Seg-1 and PhySAR-Seg-2 datasets (first three and last three rows respectively), comparing SAM-based and multimodal fusion methods. PolSAM achieves the most refined segmentation results. MVD images highlight distinct terrain properties and high-level semantic information, outperforming pseudo-colored images in this regard. However, pseudo-colored images provide richer texture details. The multi-input complementarity at feature and semantic levels is clearly demonstrated. The proposed PolSAM explicitly leverages semantic information through fusion prompts, which guide the decoder toward superior segmentation performance.

As shown in the red-boxed details, PolSAM excels at capturing edge information between different terrain classes. While LSNet Zhou et al. (2023), which incorporates edge constraints, outperforms methods without such constraints, the inherent limitations of PolSAR data, including speckle noise and unclear edges, still affect its performance. In contrast, PolSAM leverages semantic information more effectively, achieving clearer edges and superior overall segmentation accuracy.

5.3. Ablation Studies on Module Design

We perform comprehensive module ablation studies on both datasets to assess module efficacy. As shown in Table 3, we define the baseline model as original SAM using

pseudo-colored SAR images as input while training only the mask decoder. Models M1 to M5 all utilize two inputs. Compared to our method PolSAM (w/ MVD), M2, M3, and M1 validate the effectiveness of the adapter, FFP, and their combined impact respectively. The adapter in the PolSAM encoder significantly influences model performance, while the proposed FFP also improves results considerably. The effectiveness of the proposed progressive SFP is verified by comparing M4 performance. SFP module implementation enhances overall model performance, as evidenced by the results. Compared to M4, our method enhances performance by 3.97% on PhySAR-Seg-1 and 5.93% on PhySAR-Seg-2.

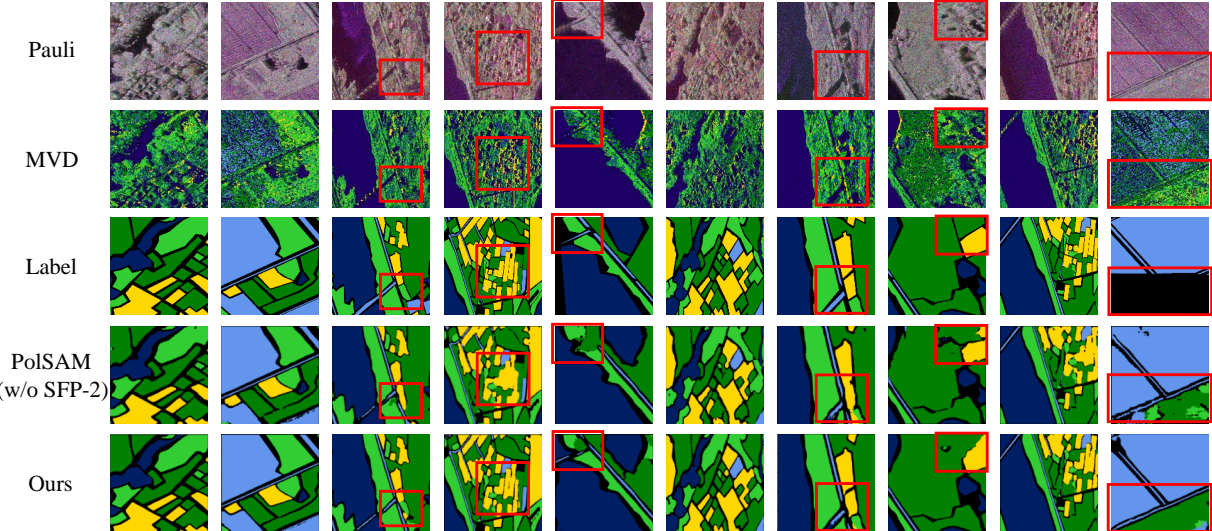
To validate the effectiveness of the progressive design of the SFP module, we conducted an additional ablation study on SFP-2, referred to as M5. The visualization results on the PhySAR-Seg-1 dataset are presented in Fig. 11. Our method, PolSAM (w/ MVD), which integrates SFP-2, significantly outperforms the version without SFP-2, especially in the details highlighted by the red box. It is important to note that the labels in the last column of images are incomplete; however, our results still accurately predict the same semantic categories as the original images. This indicates that the progressive design effectively enhances the interaction between multi-input features and high-level semantic features, enriching the semantic information embedded in the fusion prompt.

To further demonstrate our proposed method's validity, we conducted an ablation study on MVD. In the PolSAM (w/o MVD) experiment, we replaced MVD with pseudo-colored images. Despite this modification, PolSAM (w/o MVD) still shows significant improvements over the baseline, achieving mIoU increases of 15.35% on PhySAR-Seg-1 and 8.64% on PhySAR-Seg-2, illustrating the soundness of our overall model design. However, PolSAM (w/o MVD) falls short compared to PolSAM (w/ MVD). The latter

Table 3

Ablation studies on module design of PolSAM on PhySAR-Seg-1 and PhySAR-Seg-2.

	Data			Encoder			Decoder			PhySAR-Seg-1(%)			PhySAR-Seg-2(%)		
	MVD	Adapter	FFP	$PE_{1/2}$	SFP-1	SFP-2	mAcc	mF1 score	mIoU	mAcc	mF1 score	mIoU	mAcc	mF1 score	mIoU
Baseline	\times	\times	\times	\times	\times	\times	70.83	71.42	56.49	63.48	43.29	32.05			
M1	✓	\times	\times	✓	✓	✓	72.83	73.96	59.55	70.77	55.38	41.00			
M2	✓	\times	✓	✓	✓	✓	75.41	76.51	62.76	74.63	57.21	43.20			
M3	✓	✓	\times	✓	✓	✓	82.37	83.44	71.33	74.94	59.78	45.38			
M4	✓	✓	✓	\times	\times	✓	80.64	81.71	69.58	72.26	53.38	40.62			
M5	✓	✓	✓	✓	✓	✓	81.24	82.30	70.10	73.17	57.77	41.61			
PolSAM(w/o MVD)	\times	✓	✓	✓	✓	✓	82.62	83.37	71.84	73.69	59.69	45.30			
PolSAM(w/ MVD)	✓	✓	✓	✓	✓	✓	83.70	84.71	73.55	76.47	61.40	46.55			

**Figure 11:** Qualitative segmentation results on the PhySAR-Seg-1 dataset: each row displays a randomly selected image from the test set, while each column compares the outputs of different models.

achieves greater mIoU increases of 17.06% on PhySAR-Seg-1 and 9.89% on PhySAR-Seg-2 compared to the baseline, highlighting that MVD, representing scattering mechanisms, provides valuable multidimensional information that enhances segmentation performance, particularly in detail capture.

5.4. Discussions on Semantic prompt

The Effectiveness of Semantic Prompts. To verify the effectiveness of the proposed SFP, we analyze the learned ultimate sparse and dense prompt embeddings at the semantic level on the PhySAR-Seg-1 dataset, namely $\mathbf{P}_S^{(2)} \in \mathbb{R}^{N \times 256}$ and $\mathbf{P}_D^{(2)} \in \mathbb{R}^{32 \times 32 \times 256}$, where N denotes the number of sparse prompts. These embeddings reflect semantic prompts associated with class information and mask information, respectively. To better illustrate the semantic prompt, the dense prompt embedding $\mathbf{P}_D^{(2)}$ is averaged along the channel dimension, yielding $\mathbf{V}_D \in \mathbb{R}^{32 \times 32}$ for visualization. As shown in the second row of Fig. 12 (a), \mathbf{V}_D clearly highlights the semantic map corresponding to the annotated mask. Additionally, we multiply the sparse prompt embedding $\mathbf{P}_S^{(2)}$ by the dense prompt embedding $\mathbf{P}_D^{(2)}$ and average along the channel dimension to obtain the class-aware dense prompt visualization map $\mathbf{V}_{S,D}$. Notably, the class-aware prompt

reveals more discriminative semantics, as illustrated in the third row of Fig. 12 (a).

In our experiments, the number of sparse prompts C is set to the number of semantic classes. Consequently, we visualize C class-specific fusion prompt maps denoted as $\mathbf{V}_{S,D}^i, i = 1, \dots, C$ in Fig. 12 (b) for discussion. It can be observed that class-specific fusion prompt maps show significant correlation with their respective classes. The results illustrate the explicit semantic meanings of learned fusion prompts, which play important roles in guiding the decoder toward optimal segmentation results.

Sparse Prompt Parameter Selection. The number of sparse prompts N reflects the degree of semantic correlation. To evaluate its impact on model performance, we conducted ablation experiments using six different N values, each being a multiple of the dataset's category number. As shown in Table 4, optimal performance on PhySAR-Seg-1 was achieved when $N = 6$, matching the class number. Increasing N to 10 or 20 times the category number increased the model's parameter count without yielding consistent performance improvements, suggesting that excessively large N leads to parameter redundancy, while N values smaller than the class number cause semantic confusion. These results indicate that sparse prompts, when aligned

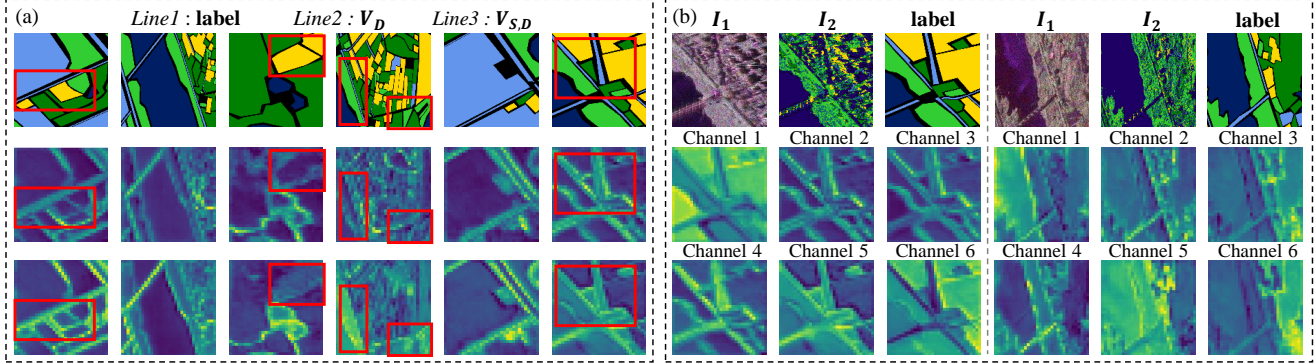


Figure 12: (a) Visualization of labels, dense prompt embedding V_D , and class-aware dense prompt embedding $V_{S,D}$. (b) Visualization of class-specific fusion prompt embedding $V_{S,D}^i$, where i corresponds to channels labeled 1–6 in the figure, representing both the channel and category indices. Pseudo-colored images I_1 , MVD I_2 , and corresponding labels are shown above.

Table 4

Ablation study on the number of sparse prompts (SP).

No. of SP	mAcc	mF1 score	mIoU
3	83.40	84.07	72.68
6 (classes)	83.70	84.71	73.55
2 * 6	82.34	83.12	71.42
4 * 6	83.43	84.29	73.01
10 * 6	83.07	83.78	72.25
20 * 6	83.37	84.28	73.06

with semantic information, facilitate effective semantic-level fusion, improving segmentation accuracy.

5.5. Discussions on Effectiveness of MVD.

Utilizing MVD offers two notable benefits. First, complex information is transformed into compact format through a series of processing stages. This process enables data to visually represent scattering mechanisms, effectively conveying physical information in an intuitively understandable manner while maintaining high correlation with semantic information. Second, MVD requires minimal memory, significantly reducing storage requirements for complex data and improving efficiency in data loading and preprocessing for neural networks.

To validate MVD effectiveness, we conducted experiments comparing different polarimetric decomposition features as MVD substitutes in PolSAM. The results in Table 5 evaluate four feature combinations, primarily based on H/A/Alpha decomposition Cloude and Pottier (1997) and the polarization coherence matrix (T). We compared performance metrics, frames per second (FPS), and data memory usage against these alternative decomposition methods.

The H/A/Alpha decomposition method Cloude and Pottier (1997) is used to analyse scattering mechanisms in PolSAR data. The entropy (H) and alpha angle (α) are calculated using the eigenvalues and eigenvectors of the coherency matrix. This allows for the characterisation of surface, double-bounce, and volume. The entropy (H) is calculated using the formula $[H = -\sum_{i=1}^3 p_i \log_3(p_i)]$,

Table 5

Ablation experiment on physical information input forms in the PhySAR-Seg-2 dataset.

Metrics (%)	Inputs: H/A/Alpha(α) / T				
	None	H/A/ α	T(6)	T(9)	H/A/ α _T
BK	29.53	33.93	33.74	32.20	32.68
Montain	64.25	74.96	66.87	63.28	65.59
Vegetation	13.23	19.90	17.81	10.34	15.02
Developed	9.21	23.12	15.48	18.21	19.73
I-urban	0.01	15.12	15.57	19.66	11.93
H-urban	18.98	31.68	26.21	20.56	31.30
L-urban	30.65	46.83	43.43	42.59	42.36
Water	90.51	91.81	94.15	93.55	93.74
mAcc	63.48	72.81	69.29	65.11	69.51
mF1 score	43.29	57.34	56.02	51.59	52.82
mIoU	32.05	42.25	39.14	37.53	39.05
FPS	26.63	22.42	12.81	7.20	5.68
Memory(GB)	-	6.49	12.99	19.46	25.9
					0.049

where p_i represents the probabilities associated with the eigenvalues. The alpha angle (α) is calculated using the formula $[\alpha = \sum_{i=1}^3 p_i \alpha_i]$, where α_i represents the corresponding scattering mechanism angles. This technique offers the benefit of offering a comprehensive explanation of scattering mechanisms, but it may be restricted by its susceptibility to noise and the assumption of simplistic scattering models, which may not accurately represent more complex ground features.

The polarization coherence matrix T is derived from the Pauli scattering vector under the reciprocity condition and represents the fully polarimetric information in PolSAR imaging Chen and Tao (2018). The matrix is given by:

$$T = \begin{bmatrix} T_{11} & T_{12} & T_{13} \\ T_{21} & T_{22} & T_{23} \\ T_{31} & T_{32} & T_{33} \end{bmatrix} = \mathbf{k}_P \mathbf{k}_P^H,$$

where $\mathbf{k}_P = \frac{1}{\sqrt{2}} [S_{HH} + S_{VV} \quad S_{HH} - S_{VV} \quad 2S_{HV}]^T$ is the Pauli scattering vector and \mathbf{k}_P^H is its conjugate transpose. The elements T_{ij} are the entries (i, j) of the matrix T , and S_{HV} denotes the rescattered return of the horizontal transmitting and

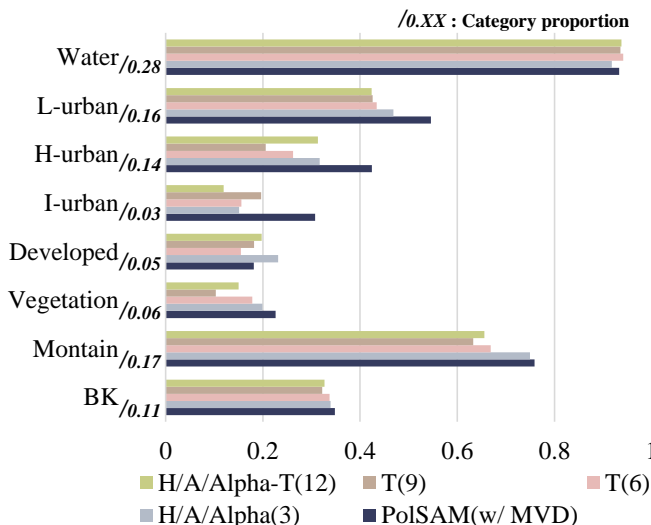


Figure 13: Impact of physical information input forms on IoU per category in the PhySAR-Seg-2 dataset.

vertical receiving polarizations. The polarization coherence matrix T is a symmetric matrix, meaning its upper triangular elements can fully represent its polarimetric features. As a result, the decomposition of T yields nine components: T_{11} , T_{22} , and T_{33} (the diagonal elements representing the power in each polarization channel), $\text{Re}[T_{12}]$, $\text{Im}[T_{12}]$ (the real and imaginary parts of the cross-polarization components), $\text{Re}[T_{13}]$, $\text{Im}[T_{13}]$ (additional cross-polarization components), and $\text{Re}[T_{23}]$, $\text{Im}[T_{23}]$ (remaining cross-polarization components).

The real parts of these upper triangular elements form the six-channel T(6) dataset, as shown in the third column of Table 5. The full set of real and imaginary components together constitute the nine-channel T(9) dataset, represented in the fourth column. Additionally, the H/A/Alpha_T(12) approach combines the three channels from the H/A/Alpha decomposition with the nine-channel data from the T decomposition, resulting in a comprehensive twelve-channel dataset.

The comparison results first demonstrate PolSAM architecture effectiveness, as all four methods incorporating different polarimetric information show improvements over the baseline, confirming model validity. Furthermore, when comparing these methods to our MVD approach, the advantages of incorporating MVD become more evident. Our MVD approach, compared to the second-best method (H/A/Alpha decomposition), shows clear improvements in evaluation metrics, with increases of 3.66% in mAcc, 4.06% in mean F1 score, and 4.3% in mIoU. These results clearly demonstrate that integrating MVD further enhances segmentation performance, highlighting its added value to the PolSAM architecture.

To further evaluate our method's effectiveness, we conducted detailed analysis of IoU metrics for each class in the PhySAR-Seg-2 dataset. The results, presented in Table 5 and visualized in Fig. 13, show that our MVD-based

method achieves optimal performance across most classes, particularly the urban class, characterized by double-bounce scattering and having the lowest dataset proportion.

For loading a batch of 668 image pairs, our method reduces loading time by 16.52 seconds, 57.11 seconds, and 82.07 seconds compared to T(6), T(9), and H/A/Alpha_T(12) approaches respectively. Regarding data storage, MVD occupies only 49 MB of memory, representing merely 0.755%, 0.377%, 0.252%, and 0.189% of the capacity utilized by the other four methods. These results highlight MVD's clear advantages, making it a highly efficient and effective option for polarimetric data processing.

6. Conclusion

In this study, we propose PolSAM, a novel segmentation framework for PolSAR image analysis. PolSAM utilizes Microwave Vision Data (MVD) representation, which encodes scattering characteristics into a lightweight and interpretable format, offering both visual and physical insights. By integrating features from pseudo-colored SAR images and MVD, PolSAM effectively combines complementary information to guide the segmentation process. The framework incorporates an FFP module for initial feature integration, supported by adapters to align representation spaces and address feature differences. Additionally, the SFP module refines segmentation through multi-level feature interactions, enabling effective incorporation of semantic and physical scattering characteristics. Together, these components enable PolSAM to achieve efficient and accurate segmentation while maintaining high interpretability.

Future work will explore more robust methods to enhance large model adaptability to SAR data for improved utilization efficiency. Additionally, considering the rich physical scattering characteristics inherent in PolSAR data, we will investigate approaches to further enhance PolSAR image segmentation results.

7. Acknowledgment

This work was supported by the National Natural Science Foundation of China (Grant No. 62571443); the National Key Laboratory of Microwave Imaging Technology; the Natural Science Basic Research Program of Shaanxi (Program No. 2025JC-QYXQ-032); and the Guangdong Basic and Applied Basic Research Foundation (Grant No. 2025A1515011368).

References

- Antropov, O., Rauste, Y., Astola, H., Praks, J., Häme, T., Hallikainen, M.T., 2013. Land cover and soil type mapping from spaceborne polsar data at l-band with probabilistic neural network. *IEEE Trans. Geosci. Remote Sens.* 52, 5256–5270.
- Bi, H., Xu, L., Cao, X., Xue, Y., Xu, Z., 2020. Polarimetric sar image semantic segmentation with 3d discrete wavelet transform and markov random field. *IEEE Trans. Image Process.* 29, 6601–6614.
- Chai, S., Jain, R.K., Teng, S., Liu, J., Li, Y., Tateyama, T., Chen, Y.w., 2023. Ladder fine-tuning approach for sam integrating complementary network. *arXiv preprint arXiv:2306.12737* .

Chen, K., Liu, C., Chen, H., Zhang, H., Li, W., Zou, Z., Shi, Z., 2024. Rsprompter: Learning to prompt for remote sensing instance segmentation based on visual foundation model. *IEEE Trans. Geosci. Remote Sens.* .

Chen, S.W., Tao, C.S., 2018. Polsar image classification using polarimetric feature-driven deep convolutional neural network. *IEEE Geosci. Remote Sens. Lett.* 15, 627–631.

Cloude, S.R., Pottier, E., 1997. An entropy based classification scheme for land applications of polarimetric sar. *IEEE Trans. Geosci. Remote Sens.* 35, 68–78.

Dong, H., Zhang, L., Zou, B., 2021. Exploring vision transformers for polarimetric sar image classification. *IEEE Trans. Geosci. Remote Sens.* 60, 1–15.

Gao, G., Bai, Q., Zhang, C., Zhang, L., Yao, L., 2023. Dualistic cascade convolutional neural network dedicated to fully polsar image ship detection. *ISPRS J. Photogramm. Remote Sens.* 202, 663–681.

Gaofen-3, 2019. Gaofen-3 (gf3) full (quad) polarimetric sample datasets. URL: <https://www.ietr.fr/GF3/>, accessed: Feb. 3, 2019.

Geng, J., Wang, R., Jiang, W., 2022. Polarimetric sar image classification based on feature enhanced superpixel hypergraph neural network. *IEEE Trans. Geosci. Remote Sens.* 60, 1–12.

Ghanbari, M., Xu, L., Clausi, D.A., 2023. Local and global spatial information for land cover semisupervised classification of complex polarimetric sar data. *IEEE J. Sel. Top. Appl. Earth Observ. Remote Sens.* 16, 3892–3904.

He, X., Wang, M., Liu, T., Zhao, L., Yue, Y., 2023. Sfaf-ma: Spatial feature aggregation and fusion with modality adaptation for rgb-thermal semantic segmentation. *IEEE Trans. Instrum. Meas.* .

Hua, W., Hou, Q., Jin, X., Liu, L., Sun, N., Meng, Z., 2024. A feature fusion network for polsar image classification based on physical features and deep features. *IEEE Geosci. Remote Sens. Lett.* .

Huang, X., Qiao, H., Zhang, B., Nie, X., 2018. Supervised polarimetric sar image classification using tensor local discriminant embedding. *IEEE Trans. Image Process.* 27, 2966–2979.

Huang, Z., Datcu, M., Pan, Z., Qiu, X., Lei, B., 2021. Hdec-tfa: An unsupervised learning approach for discovering physical scattering properties of single-polarized sar image. *IEEE Trans. Geosci. Remote Sens.* 59, 3054–3071. doi:[10.1109/TGRS.2020.3014335](https://doi.org/10.1109/TGRS.2020.3014335).

Huang, Z., Yao, X., Liu, Y., Dumitru, C.O., Datcu, M., Han, J., 2022. Physically explainable cnn for sar image classification. *ISPRS J. Photogramm. Remote Sens.* 190, 25–37.

Jamali, A., Roy, S.K., Bhattacharya, A., Ghamisi, P., 2023. Local window attention transformer for polarimetric sar image classification. *IEEE Geosci. Remote Sens. Lett.* 20, 1–5.

Jia, M., Tang, L., Chen, B.C., Cardie, C., Belongie, S., Hariharan, B., Lim, S.N., 2022. Visual prompt tuning, in: *Eur. Conf. Comput. Vis.*, Springer. pp. 709–727.

Ke, L., Ye, M., Danelljan, M., Tai, Y.W., Tang, C.K., Yu, F., et al., 2024. Segment anything in high quality. *Adv. Neural Inform. Process. Syst.* 36.

Kirillov, A., Mintun, E., Ravi, N., Mao, H., Rolland, C., Gustafson, L., Xiao, T., Whitehead, S., Berg, A.C., Lo, W.Y., et al., 2023. Segment anything, in: *Int. Conf. Comput. Vis.*, pp. 4015–4026.

Kuang, Z., Bi, H., Li, F., Xu, C., Sun, J., 2024. Polarimetry-inspired contrastive learning for class-imbalanced polsar image classification. *IEEE Trans. Geosci. Remote Sens.* .

Li, L., Ma, L., Jiao, L., Liu, F., Sun, Q., Zhao, J., 2020. Complex contourlet-cnn for polarimetric sar image classification. *Pattern Recognition* 100, 107110.

Liu, X., Jiao, L., Tang, X., Sun, Q., Zhang, D., 2018. Polarimetric convolutional network for polsar image classification. *IEEE Trans. Geosci. Remote Sens.* 57, 3040–3054.

Liu, Y., Zhang, D., Liu, N., Xu, S., Han, J., 2022. Disentangled capsule routing for fast part-object relational saliency. *IEEE Trans. Image Process.* 31, 6719–6732.

Ma, X., Wu, Q., Zhao, X., Zhang, X., Pun, M.O., Huang, B., 2024. Sam-assisted remote sensing imagery semantic segmentation with object and boundary constraints. *IEEE Trans. Geosci. Remote Sens.* .

Pu, X., Jia, H., Zheng, L., Wang, F., Xu, F., 2024. Classwise-sam-adapter: Parameter efficient fine-tuning adapts segment anything to sar domain for semantic segmentation. *arXiv preprint arXiv:2401.02326*.

Qin, R., Fu, X., Lang, P., 2020. Polsar image classification based on low-frequency and contour subbands-driven polarimetric senet. *IEEE J. Sel. Top. Appl. Earth Observ. Remote Sens.* 13, 4760–4773.

Ratha, D., Bhattacharya, A., Frery, A.C., 2017. Unsupervised classification of polsar data using a scattering similarity measure derived from a geodesic distance. *IEEE Geosci. Remote Sens. Lett.* 15, 151–155.

Reza, M.K., Prater-Bennette, A., Asif, M.S., 2024. Mmsformer: Multimodal transformer for material and semantic segmentation. *IEEE Open J. Signal Process.* .

Shen, H., Lin, L., Li, J., Yuan, Q., Zhao, L., 2020. A residual convolutional neural network for polarimetric sar image super-resolution. *ISPRS J. Photogramm. Remote Sens.* 161, 90–108.

Shi, J., He, T., Ji, S., Nie, M., Jin, H., 2023. Cnn-improved superpixel-to-pixel fuzzy graph convolution network for polsar image classification. *IEEE Trans. Geosci. Remote Sens.* .

Tirandaz, Z., Akbarizadeh, G., Kaabi, H., 2020. Polsar image segmentation based on feature extraction and data compression using weighted neighborhood filter bank and hidden markov random field-expectation maximization. *Measurement* 153, 107432.

Wang, R., Nie, Y., Geng, J., 2024. Multiscale superpixel-guided weighted graph convolutional network for polarimetric sar image classification. *IEEE J. Sel. Top. Appl. Earth Observ. Remote Sens.* .

Wang, Z., Zeng, X., Yan, Z., Kang, J., Sun, X., 2022. Air-polsar-seg: A large-scale data set for terrain segmentation in complex-scene polsar images. *IEEE J. Sel. Top. Appl. Earth Observ. Remote Sens.* 15, 3830–3841.

Wu, J., Fu, R., Fang, H., Liu, Y., Wang, Z., Xu, Y., Jin, Y., Arbel, T., 2023. Medical sam adapter: Adapting segment anything model for medical image segmentation. *arXiv preprint arXiv:2304.12620*.

Wu, W., Li, H., Li, X., Guo, H., Zhang, L., 2019. Polsar image semantic segmentation based on deep transfer learning—realizing smooth classification with small training sets. *IEEE Geosci. Remote Sens. Lett.* 16, 977–981.

Xiang, D., Ding, H., Sun, X., Cheng, J., Hu, C., Su, Y., 2024. Polsar image registration combining siamese multiscale attention network and joint filter. *IEEE Trans. Geosci. Remote Sens.* .

Xiao, D., Wang, Z., Wu, Y., Gao, X., Sun, X., 2020. Terrain segmentation in polarimetric sar images using dual-attention fusion network. *IEEE Geosci. Remote Sens. Lett.* 19, 1–5.

Xie, Z., Guan, B., Jiang, W., Yi, M., Ding, Y., Lu, H., Zhang, L., 2024. Pa-sam: Prompt adapter sam for high-quality image segmentation. *arXiv preprint arXiv:2401.13051*.

Xu, Q., Li, J., He, X., Liu, Z., Chen, Z., Duan, W., Li, C., He, M.M., Tesema, F.B., Cheah, W.P., et al., 2024a. Esp-medSAM: Efficient self-prompting sam for universal domain-generalized medical image segmentation. *arXiv preprint arXiv:2407.14153*.

Xu, Y., Tang, J., Men, A., Chen, Q., 2024b. Eviprompt: A training-free evidential prompt generation method for adapting segment anything model in medical images. *IEEE Trans. Image Process.* .

Yan, J., Xiaolan, Q., Jie, P., Songtao, S., Zezhong, W., Wei, W., Hong, Y., 2024. Mpolsar-1.0: Multidimensional sar multiband fully polarized fine classification dataset. *Lei Da Xue Bao* 13, 525–538.

Yan, Z., Li, J., Li, X., Zhou, R., Zhang, W., Feng, Y., Diao, W., Fu, K., Sun, X., 2023. Ringmo-sam: A foundation model for segment anything in multimodal remote-sensing images. *IEEE Trans. Geosci. Remote Sens.* 61, 1–16.

Yu, L., Zeng, Z., Liu, A., Xie, X., Wang, H., Xu, F., Hong, W., 2022. A lightweight complex-valued deeplabv3+ for semantic segmentation of polsar image. *IEEE J. Sel. Top. Appl. Earth Observ. Remote Sens.* 15, 930–943.

Yue, W., Zhang, J., Hu, K., Wu, Q., Ge, Z., Xia, Y., Luo, J., Wang, Z., 2023. Part to whole: Collaborative prompting for surgical instrument segmentation. *arXiv preprint arXiv:2312.14481*.

Yue, W., Zhang, J., Hu, K., Xia, Y., Luo, J., Wang, Z., 2024. SurgicalSAM: Efficient class promptable surgical instrument segmentation, in: *AAAI Conf. Art. Intell.*, pp. 6890–6898.

Zeng, X., Wang, Z., Feng, K., Gao, X., Sun, X., 2022. Ts-shes: Terrain segmentation in complex-valued polsar images via scattering harmonization and explicit supervision. *IEEE Trans. Geosci. Remote Sens.* 60, 1–20.

Zeng, X., Wang, Z., Wang, Y., Rong, X., Guo, P., Gao, X., Sun, X., 2023. Semipscn: Polarization semantic constraint network for semi-supervised segmentation in large-scale and complex-valued polsar images. *IEEE Trans. Geosci. Remote Sens.* .

Zhang, C., Han, D., Qiao, Y., Kim, J.U., Bae, S.H., Lee, S., Hong, C.S., 2023a. Faster segment anything: Towards lightweight sam for mobile applications. *arXiv preprint arXiv:2306.14289* .

Zhang, D., Huang, G., Zhang, Q., Han, J., Han, J., Wang, Y., Yu, Y., 2020a. Exploring task structure for brain tumor segmentation from multi-modality mr images. *IEEE Trans. Image Process.* 29, 9032–9043.

Zhang, D., Li, H., Zeng, W., Fang, C., Cheng, L., Cheng, M.M., Han, J., 2023b. Weakly supervised semantic segmentation via alternate self-dual teaching. *IEEE Trans. Image Process.* .

Zhang, J., Liu, H., Yang, K., Hu, X., Liu, R., Stiefelhagen, R., 2023c. Cmx: Cross-modal fusion for rgb-x semantic segmentation with transformers. *IEEE Trans. Intell. Transp. Syst.* .

Zhang, J., Yang, X., Jiang, R., Shao, W., Zhang, L., 2024a. Rsam-seg: A sam-based approach with prior knowledge integration for remote sensing image semantic segmentation. *arXiv preprint arXiv:2402.19004* .

Zhang, L., Zhang, S., Zou, B., Dong, H., 2020b. Unsupervised deep representation learning and few-shot classification of polsar images. *IEEE Trans. Geosci. Remote Sens.* 60, 1–16.

Zhang, Q., He, C., He, B., Tong, M., 2023d. Learning scattering similarity and texture-based attention with convolutional neural networks for polsar image classification. *IEEE Trans. Geosci. Remote Sens.* 61, 1–19.

Zhang, R., Jiang, Z., Guo, Z., Yan, S., Pan, J., Ma, X., Dong, H., Gao, P., Li, H., 2023e. Personalize segment anything model with one shot. *arXiv preprint arXiv:2305.03048* .

Zhang, Y., Cheng, T., Hu, R., Liu, H., Ran, L., Chen, X., Liu, W., Wang, X., et al., 2024b. Evf-sam: Early vision-language fusion for text-prompted segment anything model. *arXiv preprint arXiv:2406.20076* .

Zheng, L., Pu, X., Xu, F., 2024. Tuning a sam-based model with multi-cognitive visual adapter to remote sensing instance segmentation. *arXiv preprint arXiv:2408.08576* .

Zhou, W., Liu, J., Lei, J., Yu, L., Hwang, J.N., 2021. Gmnet: Graded-feature multilabel-learning network for rgb-thermal urban scene semantic segmentation. *IEEE Trans. Image Process.* 30, 7790–7802.

Zhou, W., Zhu, Y., Lei, J., Yang, R., Yu, L., 2023. Lsnet: Lightweight spatial boosting network for detecting salient objects in rgb-thermal images. *IEEE Trans. Image Process.* 32, 1329–1340.

Zhou, X., Liang, F., Chen, L., Liu, H., Song, Q., Vivone, G., Chanussot, J., 2024. Mesam: Multiscale enhanced segment anything model for optical remote sensing images. *IEEE Trans. Geosci. Remote Sens.* 62, 1–15.